Planning the Collision-Free Paths of an Actively Flexible Manipulator

José Bañón
Robotics Laboratory
Department of Computer Science, Stanford University
Stanford, CA 94305, USA

Abstract

Most robot manipulators consist of a small sequence of rigid links connected by articulated joints. However, robot dexterity is considerably enhanced when the number of joints is large or infinite. Additional joints make it possible to manipulate objects in cluttered environments where non-redundant robots are useless. In this paper we consider a simulated actively flexible manipulator (AFM), *i.e.* a manipulator whose flexibility can be directly controlled by its actuators. We propose an efficient method for planning the collision-free paths of an AFM in a three-dimensional workspace. We implemented this method on a graphic workstation and experimented with it on several examples.

Acknowledgments: This research was supported in part by DARPA under Contract DAA21-89-C0002 (Army). José Bañon[1] was supported by a Fullbright fellowship. I would like to thank to Jean-Claude Latombe, who helped a lot in improving the paper.

[1]Present address: Departamento de Ciencias de la Computación, Facultad de Ingeniería, Universidad del Valle, Cali, Colombia. E-mail: banon@mafalda.univalle.edu.co.

1 Introduction

Most robot manipulators consist of a finite, usually small, sequence of rigid links connected by revolute and/or prismatic joints. However, it is well-known that robot dexterity is considerably increased when the number of its degrees of freedom is large or infinite. Additional degrees of freedom make it possible to manipulate objects in a cluttered environment where a non-redundant robot would be useless, *e.g.* a cooling pipe environment (such as in a nuclear power plant), a complex frame structure (such as in a space platforms), and a tubular environment (for instance, during a pipe inspection task). Although highly redundant manipulators are more difficult to design and build, this issue has been addressed in several papers (*e.g.*, [1, 2, 3, 5, 6]). Prototypes have already been built and new ones are being built. For example, a highly redundant manipulator made up of successive Stewart platforms is described in [8]. Recently, a three-degree-of-freedom flexible microactuator driven by an electro-pneumatic system has been developed [9]. Our own laboratory currently builds a flexible arm whose apparence is that of a narrow accordion bellows, with each folding having two degrees of freedom.

In this paper we consider a simulated "actively" flexible manipulator (AFM), *i.e.* a manipulator whose flexibility can be directly controlled by its actuators. This type of manipulator differs from the "passively" flexible manipulators whose flexibility is not directly controllable, but results from the fact that the links are constructed using light-weight materials [10, 11, 12, 13]. Our manipulator is modeled as a cylinder whose spine is a curved line segment of fixed length. One end of the spine is fixed, while the other carries an end-effector in a three-dimensional workspace. We assume that the curvature and the torsion of the spine at any point can be set by the actuators as one wishes. One can get a feeling of the nature of an AFM by considering it as the limit of an ordinary revolute-joint manipulator in which the length of every link tends toward zero, while the number of joints (and links) tends toward infinity. An AFM is sometimes called a "snake" or "elephant-trunk" robot.

We propose new efficient techniques for planning collision-free paths for an AFM in a three-dimensional workspace. These techniques have been implemented in a planner running on a Silicon Graphic workstation, and we have experimented with them using several examples, including a simplified pipe manipulation example reported in this paper. Although investigating motion planning for AFM's has been the primary purpose of our research, a significant portion of this paper is devoted to the inverse kinematic problem. The reason is that the planner exploits the kinematic structure of the AFM by essentially generating a collision-free path for the end-effector and letting the rest of the manipulator follow the same path. This approach requires the inverse kinematics problem to be solved efficiently.

So far, most of the research in robot motion planning has been conducted with robots consisting of a small number of rigid links [14]. Recently, however, an approach combining potential field and randomized search techniques has been developed and successfully applied to highly redundant robots, including a simulated serial manipulator with 31 degrees of freedom [15]. This approach is fairly general and has been applied to robots with very different kinematic structures, including rigid bodies in 2D and 3D workspaces, collection of independent rigid bodies, planar and spatial manipulators, serial, star-shaped and closed-loop kinematic chains. But it does not apply to AFM's. The approach to motion planning presented below is much more specific in that it exploits the kinematic properties of the

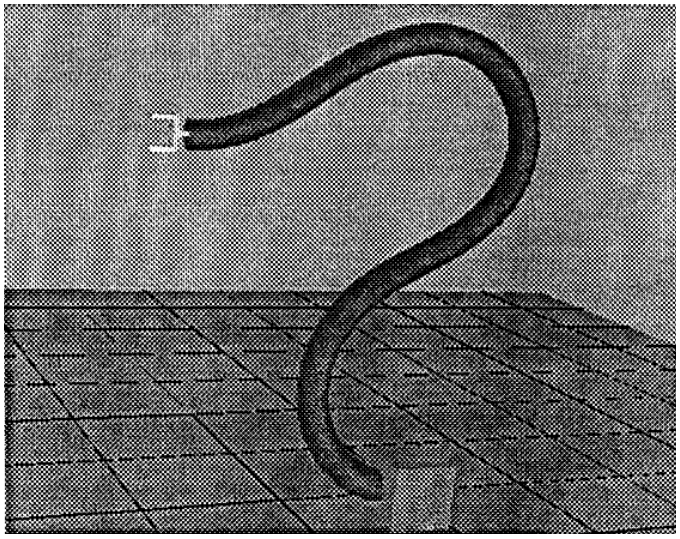

Figure 1: Simulated AFM

AFM's structure. On the other hand, it may be a very efficient alternative to the method of [15] for dealing with highly redundant robots with revolute joints, by approximating such robots by AFMs whenever this is realistic.

Planning motion methods and inverse kinematics technics are now available for research in computer animation. The inverse kinematics technics have been successfully employed to control motion in graphics animation of articulated figures [16, 17]. Very little work has been done in using inverse kinematics technics in animating flexible objects which are often treated by large collection of differential equation subject to reach a goal and to satisfy some constraints [18, 19]. The techniques described in this paper can be applied to generate graphics animation of flexible objects.

The paper is organized as follows. In Section 4 we introduce the notion of an AFM, we formulate the motion planning problem for such a manipulator, and we outline the main ideas underlying our planning approach. In Section 5 we develop the concept of a helix-like AFM and we present its direct and inverse kinematics. In Section 6 we state three important properties of helix-like AFM that are the basis of our planning method. This method consists of three main steps. In Sections 7, 8, and 9 we describe these steps in detail. In Section 10 we present the implemented planner and we show experimental results. Most of the mathematical developments are omitted in the main text and are given in appendices.

2 Notion of an AFM

We model an AFM as a curved cylinder obtained by sweeping a constant circular cross-section perpendicular to a curve segment. This segment is called the *spine* of the AFM. One end of the cylinder is fixed and the other carries an end-effector. A display of the AFM is shown in Figure 1.

The spine is described as a regular parameterized curve of fixed length L in $\mathbf{R}^3$. Such a curve is defined by a differentiable function $\mathbf{r} : I \longrightarrow \mathbf{R}^3$ which assigns a position $\mathbf{r}(s) \in \mathbf{R}^3$ to each $s \in I = [s_0, s_1]$. The function $\mathbf{r}(.)$ is called the *configuration* of the AFM.

The coordinates of $\mathbf{r}(s)$ are expressed in a fixed coordinate system attached to the workspace. The fixed end of the manipulator corresponds to $s = s_0$ and the moving end to $s = s_1$. Without loss of generality, we assume that the AFM's fixed end is at the origin of the workspace coordinate system (Figure 1) and that s is the arc-length of the spine section connecting $\mathbf{r}(0)$ to $\mathbf{r}(s)$. Hence, $s_0 = 0$, $s_1 = L$, and $\mathbf{r}(0) = (0, 0, 0)$.

In the following, we let $\mathcal{C}_L$ denote the *configuration space* of an AFM of length L, *i.e.* the set of all functions $\mathbf{r}(.)$ defined as above.

The *tangent* to the spine is the vector function:[2]

$$\mathbf{T}(s) = \mathbf{r}'(s). \tag{1}$$

Since s designates the length of the spine, we have $||\mathbf{T}(s)|| = 1$. The *normal* $\mathbf{N}(s)$ and the *binormal* $\mathbf{B}(s)$ vectors are defined by:

$$\begin{aligned} \mathbf{N}(s) &= \mathbf{T}'(s)/||\mathbf{T}'(s)||, && (2) \\ \mathbf{B}(s) &= \mathbf{T}(s) \wedge \mathbf{N}(s). && (3) \end{aligned}$$

For each value of s, the *Frenet trihedron* $\{\mathbf{T}(s), \mathbf{N}(s), \mathbf{B}(s)\}$ constitutes an orthogonal reference system attached to the spine at the point of arc-length s. The rate of change of such a reference system is expressed by the following *Frenet equations*, which describe the local behavior of the AFM's spine [7]:

$$\begin{aligned} \mathbf{T}'(s) &= \kappa(s)\ \mathbf{N}(s), && (4) \\ \mathbf{N}'(s) &= -\kappa(s)\ \mathbf{T}(s) + \tau(s)\ \mathbf{B}(s), && (5) \\ \mathbf{B}'(s) &= -\tau(s)\ \mathbf{N}(s). && (6) \end{aligned}$$

The scalar quantities $\kappa(s)$ and $\tau(s)$ are called the *curvature* and the *torsion* of the spine, respectively. The curvature represents the rate of change of the direction of the tangent with respect to the arc length. The torsion, also called the *second curvature*, measures how rapidly the spine pulls away from the *osculating plane*, which is the plane determined by its tangent and normal. The *fundamental existence and uniqueness theorem* for space curves asserts that a regular curve is completely determined, up to a rigid-body transform, by its curvature and torsion.

We call $\mathbf{r}(L)$, $\mathbf{T}(L)$, and $(\mathbf{r}(L), \mathbf{T}(L))$ the *position*, *orientation*, and *configuration* of the AFM's end-effector, respectively. We assume that the AFM's actuators can tune the curvature and the torsion of the spine at every $s \in [0, L]$ as one desires. Hence, by selecting $\kappa(s)$ and $\tau(s)$ appropriately, one may achieve desired values of the configuration of the end-effector. We also assume that the actuators allow the orientation $\mathbf{T}(0)$ to be set as one wishes.

[2] Throughout this paper $f'(s)$ and $f''(s)$ denote the first and second derivatives of $f(s)$. The "prime" and "double-prime" symbols are used in no other circumstances.

3 Planning Problem

We consider the problem of planning a collision-free path for an AFM in a three-dimensional workspace that contains fixed obstacles, from an *initial configuration* $\mathbf{r}_I(.)$ to a *goal configuration* such that the end-effector is at a given desired configuration $(\mathbf{r}_G, \mathbf{T}_G)$. (Any collision-free configuration $\mathbf{r}(.)$ verifying $\mathbf{r}(L) = \mathbf{r}_G$ and $\mathbf{r}'(L) = \mathbf{T}_G$ is a goal configuration of the AFM.)

A solution to such a problem is a continuous map:

$$u \in [0,1] \mapsto \mathbf{r}(u,.) = \mathbf{r}_u(.) \in \mathcal{C}_L,$$

called a *path*, such that:
- $\mathbf{r}_0(.) = \mathbf{r}_I(.)$, $\mathbf{r}_1(L) = \mathbf{r}_G$ and $\mathbf{r}'_1(L) = \mathbf{T}_G$,
- for every $u \in [0,1]$, $\mathbf{r}_u(.)$ is a collision-free configuration of the AFM.

For simplification, we will assume that the radius of the AFM's cross-section is zero, *i.e.* that the AFM reduces to its spine, and that the end-effector is dimensionless, *i.e.* that it reduces to the point $\mathbf{r}(L)$. One can easily deal with a non-zero cross-section by "growing" every obstacle isotropically by the radius of the cross-section.

4 Planning Approach

We propose a path planning approach based on the assumption that the workspace can be divided into two half-spaces, $\mathcal{W}_0$ and $\mathcal{W}_1$, separated by a plane $\mathcal{P}$ (that we will choose perpendicular to the x-axis of the coordinate system). We assume that all the obstacles are in $\mathcal{W}_1$, and that there exist configurations of the AFM that are completely contained in $\mathcal{W}_0$. We call $\mathcal{W}_0$ the *maneuvering region* and $\mathcal{W}_1$ the *working region*.

Our planning approach essentially consists of planning a collision-free path of the AFM's end-effector in the working region, letting the part of the AFM's body in the working region follow that path (in the same way as the body of a snake follows the path of the snake's head), and managing the rest of the AFM's body so that it lies entirely in the maneuvering region. We therefore decompose the input planning problem into two subproblems: planning in the working region $\mathcal{W}_1$ and planning in the maneuvering region $\mathcal{W}_0$. In the maneuvering region, the path of the AFM is generated by giving the AFM a convenient helix-like shape whose inverse kinematics can be analytically computed (see Section 5). In the working region, the AFM must avoid collision with the obstacles; the path is generated using a classical cell decomposition path planning method.

Let us first consider the case where the initial configuration $\mathbf{r}_I(.)$ is a helix-like curve lying entirely in the maneuvering region $\mathcal{W}_0$ and the goal position $\mathbf{r}_G$ of the end-effector is located in the working region $\mathcal{W}_1$. Our planning approach operates according to the following three steps:

1. A smooth collision-free curve $\mu : [0,1] \rightarrow \mathbf{R}^3$ is generated which joins a point $\mathbf{r}_\mathcal{P}$ selected in $\mathcal{P}$ to the point $\mathbf{r}_G$, with the tangent $\mu'(1)$ pointing along the desired goal orientation $\mathbf{T}_G$. The point $\mathbf{r}_\mathcal{P}$ is where the AFM will traverse the plane $\mathcal{P}$.

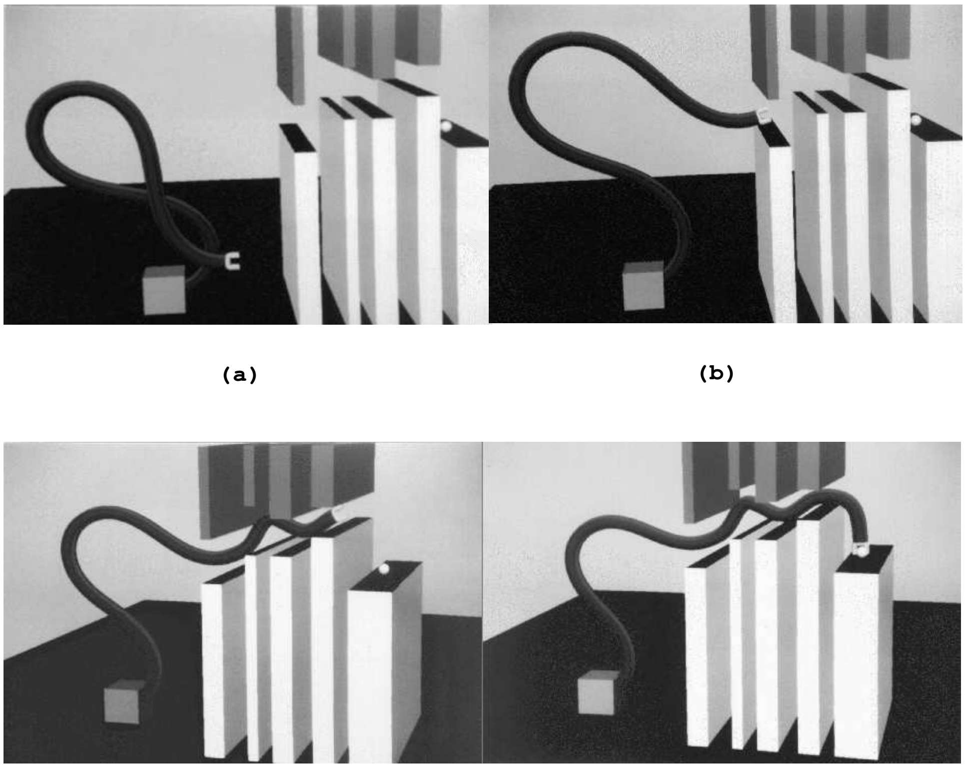

(a) (b)

(c) (d)

Figure 2: Path generated by the planner

2. Let $\mathbf{T}_{\mathcal{P}}$ be the unit vector pointing along the tangent to μ at $\mathbf{r}_{\mathcal{P}}$. A path π_1 of the AFM is generated between the initial configuration $\mathbf{r}_I(.)$ and an intermediate configuration $\mathbf{r}_{\mathcal{P}}(.)$ such that $\mathbf{r}_{\mathcal{P}}(L) = \mathbf{r}_{\mathcal{P}}$ and $\mathbf{r}'_{\mathcal{P}}(L) = \mathbf{T}_{\mathcal{P}}$. All configurations along π_1 lie in the maneuvering region and have a helix-like shape.

3. A path π_2 of the AFM is generated between the intermediate configuration $\mathbf{r}_{\mathcal{P}}(.)$ and a goal configuration. It is constructed by making the end-effector track the portion of μ that is contained in $\mathcal{W}_1$, with the portion of the AFM contained in $\mathcal{W}_1$ coinciding with the portion of μ connecting $\mathbf{r}_{\mathcal{P}}$ to the current position of the end-effector. The portion of the AFM lying in $\mathcal{W}_0$ keeps a helix-like shape.

The concatenation of π_1 and π_2 is a collision-free path achieving the goal configuration of the end-effector from the initial configuration of the AFM. Figure 2 shows such a path generated by our planner. The working region contains various parallelepipedic obstacles placed on top of the working table or hanging from above. The task of the AFM is to reach a ball (shown white) located on the rightmost obstacle. Figure 2.a displays the helix-like AFM at its initial configuration in the maneuvering region. Figure 2.b shows the AFM when the end-effector enters the working region. Figure 2.*c* displays a configuration where part of the AFM is in the working region. Figure 2.*d* shows the AFM when the end-effector reaches the goal.

If both the initial position $\mathbf{r}_I(L)$ and the goal position $\mathbf{r}_G$ of the end-effector are located in the working region $\mathcal{W}_1$, the planner first selects an arbitrary helix-like configuration $\mathbf{r}_m(.)$ entirely contained in the maneuvering region. Next, it generates two paths, the first connecting $\mathbf{r}_I(.)$ to $\mathbf{r}_m(.)$, the second achieving the goal configuration of the end-effector from $\mathbf{r}_m(.)$. Both paths are constructed using the above three-step approach.

The three steps will be described in detail in Sections 7 (generation of π_1), 8 (generation of μ), and 9 (generation of π_2). Let us first develop the concept of a helix-like AFM.

5 Notion of a Helix-Like AFM

5.1 Definition

In general, in three dimensions, the Frenet equations of an AFM form a system of linear homogeneous differential equations whose solutions cannot be obtained in integral form as is the case for planar curves. One way to make these equations integrable is to restrict the AFM to a helix-like curve.

A *helix-like* curve is a regular curve whose torsion is proportional to the curvature, *i.e.* such that $\tau(s) = C\kappa(s)$, where C is a non-zero constant except when the curve is planar. There then exists a fixed vector $\mathbf{A}$ in $\mathbf{R}^3$, called the *axis* of the helix-like curve, whose angle with the tangent vector $\mathbf{T}(s)$ is constant for all values of s. In order to simplify mathematical expressions, and without loss of generality, we temporarily assume that $\mathbf{A}$ points along the z-axis of the workspace coordinate system.

The tangent to the helix-like curve is then a vector of the form:

$$\mathbf{T}(s) = (a\cos\theta(s), \quad a\sin\theta(s), \quad b), \tag{7}$$

where the quantity b is equal to the cosine of the constant angle between the z-axis and $\mathbf{T}(s)$, and $a = \pm\sqrt{1-b^2}$. The angle $\theta(s)$ is the angle that the projection of $\mathbf{T}(s)$ into the xy-plane makes with the x- axis.

One can verify that the curvature and the torsion satisfy the equations:

$$\kappa(s) = a\theta'(s) \quad \text{and} \quad \tau(s) = b\theta'(s), \tag{8}$$

respectively. Therefore, $C = b/a = \pm b/\sqrt{1-b^2}$.

The arc-length parameterized equation of the helix-like curve is given by the following integral expression:

$$\mathbf{r}(s) = (a\int_0^s \cos\theta(u)du, \quad a\int_0^s \sin\theta(u)du, \quad b\ s). \tag{9}$$

A nice property of this helix model is that autocollision cannot occur when $b \neq 0$. This is a very desirable property, since an AFM usually has a large range of motion capabilities in $\mathbf{R}^3$. An autocollision checking routine typically requires a significant amount of computation, which would slow down the motion planner. When $b = 0$, the AFM becomes the planar manipulator studied in [2]; in this case only, it may reach autocollision configurations.

5.2 Direct Kinematics

We wish to compute the coordinates (x, y, z) and the direction cosines (c_1, c_2, c_3), defining the position $\mathbf{r}(L)$ and orientation $\mathbf{T}(L)$ of the end-effector in the workspace coordinate system, given the values of the curvature and the torsion along the AFM's spine.

Because the Frenet equations are not integrable in general, we already restricted the shape of the AFM's spine to be a helix-like curve segment. This yields the integral form of $\mathbf{r}(s)$ given in Equ. (9). But it is still not always possible to find an analytical solution. Although we could use numerical integration techniques, another approach is possible, which was originally proposed in [2] for a planar AFM. In the planar case it consists of restricting the AFM's curvature to a linear combination of some independent functions yielding an analytic solution for the integral form of $\mathbf{r}(s)$. We simply extend this approach to the three-dimensional case by expressing both the curvature and the torsion as linear combinations of N predefined independent *mode functions* $\psi_i(s)$:

$$\kappa(s) = \sum_{i=1}^{N} \alpha_i \psi_i(s) \quad \text{and} \quad \tau(s) = \sum_{i=1}^{N} \beta_i \psi_i(s). \tag{10}$$

The parameters α_i and β_i determine the curvature and the torsion of the AFM. They now constitute the actual degrees of freedom of the manipulator. With a helix-like curve of constant C, we have $\beta_i/\alpha_i = C$ for all $i \in [1, N]$.

We apply this approach with:

$$\kappa(s) = a(a_1 \cos\frac{2\pi s}{L} + a_2 \sin\frac{2\pi s}{L}) \quad \text{and} \quad \tau(s) = C\ \kappa(s). \tag{11}$$

(The same modal expansion was used in [2] for the curvature.) We can restrict a to be positive or null, since changing the sign of a is equivalent to changing the sign of both a_1 and a_2. Hence:

$$a = +\sqrt{1 - b^2}. \tag{12}$$

This choice also entails $C = +b/\sqrt{1 - b^2}$. Therefore, at this stage, the degrees of freedom of the AFM have been reduced to three parameters: a_1, a_2, and b.

By integrating the equation $\kappa(s) = a\theta'(s)$, we obtain:

$$\theta(s) = \frac{a_1 L}{2\pi} \sin\frac{2\pi s}{L} + \frac{a_2 L}{2\pi}(1 - \cos\frac{2\pi s}{L}) + \theta_0, \tag{13}$$

where θ_0 is the angle that the projection of $\mathbf{T}(0) = \mathbf{T}(L) = (a\cos\theta_0, a\sin\theta_0, b)$ into the xy-plane makes with the x-axis. We assume that θ_0 can be tuned as one wishes. Hence, it is an additional degree of freedom that rotates the orientation of the end-effector $\mathbf{T}(L)$ about the axis of the helix-like curve. Since the parameter b is used to achieve the z coordinate of $\mathbf{r}(L)$, it is clear that we need another parameter to achieve an arbitrary orientation $\mathbf{T}(L)$ of the end-effector. This can be done by allowing the axis $\mathbf{A}$ to rotate about the y-axis. Let $\mathcal{R}_y(\varphi)$ denote the rotation of angle φ about the y-axis. Then the position and orientation of the end-effector becomes $\mathcal{R}_y(\varphi)\ \mathbf{r}(L)$ and $\mathcal{R}_y(\varphi)\ \mathbf{T}(L)$, respectively. The case where $\varphi = 0$ is when $\mathbf{A}$ points along the z- axis.

Substituting the expression (13) in Equ. (9) and integrating, we obtain the coordinates and the direction cosines of the end-effector of the AFM:

$$\mathbf{r}(L) = \begin{pmatrix} \cos\varphi & 0 & \sin\varphi \\ 0 & 1 & 0 \\ -\sin\varphi & 0 & \cos\varphi \end{pmatrix} \begin{pmatrix} \cos\theta_0 & -\sin\theta_0 & 0 \\ \sin\theta_0 & \cos\theta_0 & 0 \\ 0 & 0 & 1 \end{pmatrix} \begin{pmatrix} a\tilde{x} \\ a\tilde{y} \\ bL \end{pmatrix}, \tag{14}$$

$$\mathbf{T}(L) = \begin{pmatrix} \cos\varphi & 0 & \sin\varphi \\ 0 & 1 & 0 \\ -\sin\varphi & 0 & \cos\varphi \end{pmatrix} \begin{pmatrix} a\cos\theta_0 \\ a\sin\theta_0 \\ b \end{pmatrix}, \tag{15}$$

with:

$$\tilde{x} = L\ \cos(\frac{a_2 L}{2\pi})\ J_0(\frac{L}{2\pi}\sqrt{a_1^2 + a_2^2}), \tag{16}$$

$$\tilde{y} = L\ \sin(\frac{a_2 L}{2\pi})\ J_0(\frac{L}{2\pi}\sqrt{a_1^2 + a_2^2}), \tag{17}$$

where $a = +\sqrt{1-b^2}$ (Equ. 12) and J_0 denotes the Bessel function of order zero. The derivation of these equations makes use of orthogonality properties and identities involving Bessel functions. (Details can be found in [1].)

Therefore, the values of the five *state parameters* a_1, a_2, b, θ_0 and φ completely determine the position and orientation of the end-effector. We call the vector $\xi = (a_1, a_2, b, \theta_0, \phi)$ the *state vector* of the AFM..

In the particular case where $\theta_0 = \varphi = 0$, the direct kinematic equations simplify to:

$$x = a\ L\ \cos(\frac{a_2 L}{2\pi})\ J_0(\frac{L}{2\pi}\sqrt{a_1^2 + a_2^2}), \tag{18}$$

$$y = a\ L\ \sin(\frac{a_2 L}{2\pi})\ J_0(\frac{L}{2\pi}\sqrt{a_1^2 + a_2^2}), \tag{19}$$

$$z = b\ L. \tag{20}$$

We then have:

$$T(L) = T(0) = (\sqrt{1-b^2}, 0, b). \tag{21}$$

Direct kinematics computation can be cut by one half by noticing that the second half of the AFM derives from the first half by applying a translation, a rotation, and reflexion to it (see Appendix A).

5.3 Inverse Kinematics

The inverse kinematics problem is to determine the state vector ξ in order to achieve a desired position (x, y, z) and orientation (c_1, c_2, c_3) of the end-effector.

¿From Equ. (14) and (15), we can compute a_1, a_2, b, θ_0 and φ as functions of x, y, z, c_1, c_2 and c_3. This computation, which is developed in Appendix B, yields the following closed-form expressions for the inverse kinematics:

$$\varphi = \arctan\frac{z - Lc_3}{Lc_1 - x}, \tag{22}$$

$$\begin{aligned}
b &= c_1 \sin\varphi + c_3 \cos\varphi, && (23)\\
\theta_0 &= \arcsin \frac{c_2}{a}, && (24)\\
a_2 &= \frac{2\pi}{L} \arcsin \frac{y}{\sqrt{x^2+y^2+z^2-(Lb)^2}} - \frac{2\pi}{L}\theta_0, && (25)\\
a_1 &= \pm\sqrt{\left(\frac{2\pi}{L}\right)^2 \left(J_0^{-1}\left(\sqrt{\frac{x^2+y^2+z^2-(Lb)^2}{(La)^2}}\right)\right)^2 - a_2^2}, && (26)
\end{aligned}$$

where $a = +\sqrt{1-b^2}$. In the particular case where $\theta_0 = \varphi = 0$, these equations reduce to:

$$\begin{aligned}
b &= \frac{z}{L}, && (27)\\
a_2 &= \frac{2\pi}{L} \arcsin \frac{y}{\sqrt{x^2+y^2}}, && (28)\\
a_1 &= \pm\sqrt{\left(\frac{2\pi}{L}\right)^2 \left(J_0^{-1}\left(\sqrt{\frac{x^2+y^2}{(La)^2}}\right)\right)^2 - a_2^2}. && (29)
\end{aligned}$$

In order to define a unique inverse Bessel function J_0^{-1}, we have to restrict the function $J_0(u)$ to the interval $u \in [0, \mu_0]$, where $\mu_0 \approx 2.405$ is the first zero of J_0. Then the inverse function $J_0^{-1} : [0,1] \mapsto [0, \mu_0]$ is a monotonically decreasing function. It is calculated using numerical tables and linear interpolation techniques.

This restriction of the range of values of u is not a limitation of the applicability of the above equations. Indeed, the definition domain of the inverse Bessel function J_0^{-1} is the interval $[0,1]$, which implies:

$$0 \leq \sqrt{\frac{x^2+y^2+z^2-(Lb)^2}{(La)^2}} \leq 1. \qquad (30)$$

Using the relation $a^2+b^2=1$, this condition is equivalent to $0 \leq x^2+y^2+z^2 \leq L^2$, which simply expresses the already known fact that the locus of the end- effector is included in a sphere of radius L. However, the restriction of u to $[0, \mu_0]$ entails the following upper-bounds for the curvature and the torsion:

$$|\kappa_{max}| < \frac{4\pi\mu_0}{L} \quad \text{and} \quad |\tau_{max}| < \frac{4\pi\mu_0}{L}. \qquad (31)$$

Indeed, the values of a_1 and a_2 are then constrained by $0 \leq (a_1^2 + a_2^2) \leq (2\pi\mu_0/L)^2$.

In order for the parameter a_1 to be real, it is necessary that:

$$J_0^{-1}\left(\sqrt{\frac{x^2+y^2+z^2-(Lb)^2}{(La)^2}}\right) \geq |a_2| \frac{L}{2\pi}. \qquad (32)$$

This equation requires that the x, y, and z coordinates of the end-effector be inside a bounded volume, called the *reachable volume*. In the following we will only use the subset

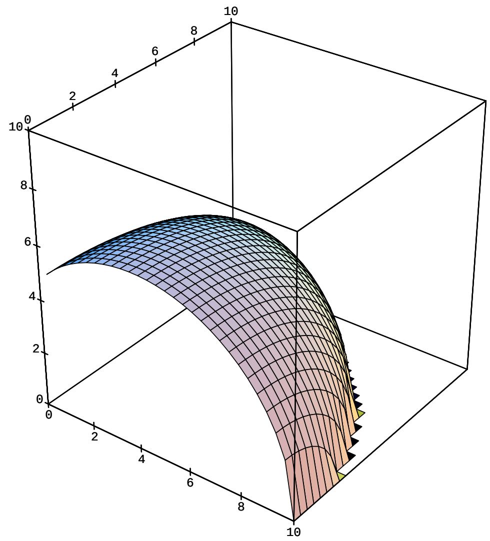

Figure 3: Reachable volume $\mathcal{V}$

of this volume that is contained in the quarter-space $\{x \geq 0\} \cap \{y \geq 0\}$ Let $\mathcal{V}$ designate this subset when $\theta_0 = \varphi = 0$. $\mathcal{V}$ is represented in Figure 3 for $z \geq 0$; the other half, for $z \leq 0$, is symmetrical. $\mathcal{V}$ is a convex set.

Since the position of the end-effector is a function of the square of a_1 (see Equ. (16) and (17)), changing the sign of a_1 with the same values of the other state parameters yields the same end-effector's position. Both expressions of a_1 in Equ. (26) are valid solutions of the inverse kinematic equations, but they produce different configurations $\mathbf{r}(.)$ of the AFM. In the following, we will always use the solution in which $a_1 \geq 0$.

Figure 4 shows several configurations along a path where the end-effector translates at constant orientation. Figure 5 illustrates a path where the end-effector changes orientation at fixed position. Both paths were computed using the above inverse kinematic equations.

6 Properties of a Helix-Like AFM

We now state three properties of helix-like curves, which are used by our planner. Their proofs are given in Appendixes D, F, and G, respectively.

Property 1: *Let $\theta_0 = 0$. Let $y(s)$ denote the y coordinate of $\mathbf{r}(s)$. If $y(L) \geq 0$, then $y(s) \geq 0$ for all $s \in [0, 1]$.*

This property allows us to install the AFM on top of a horizontal table whose upper surface is slightly below the plane $y = 0$. Then, as long as $\theta_0 = 0$, we do not have to worry about collisions between the AFM and the table.

Property 2: *Let $\theta_0 = 0$ and $\varphi = 0$. Let $x(s)$ denote the x coordinate of $\mathbf{r}(s)$. If $x(L) \leq L/2$, then $x(s) \leq L/2$ for all $s \in [0, 1]$.*

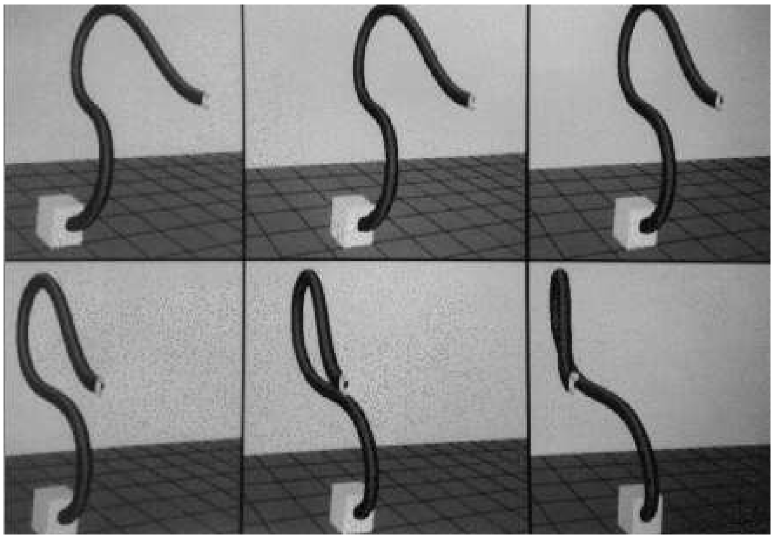

Figure 4: Translation of the end-effector

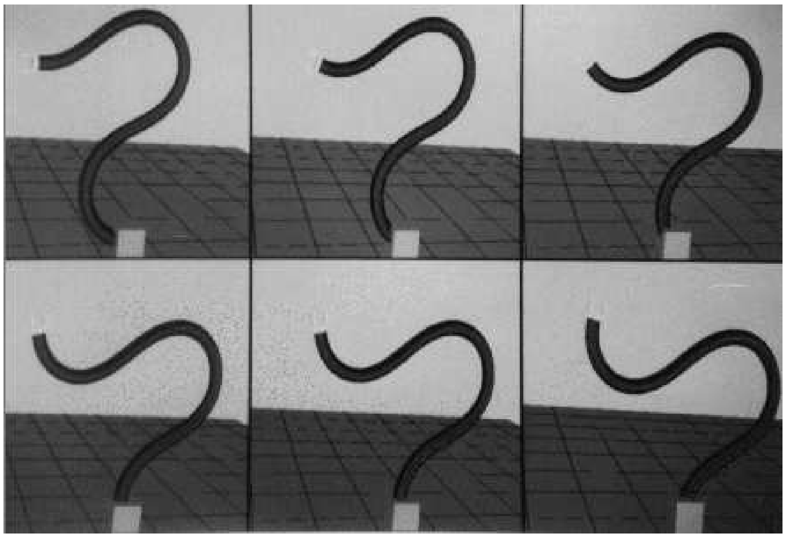

Figure 5: Rotation of the end-effector

Remember that the maneuvering region $\mathcal{W}_0$ and the working region $\mathcal{W}_1$ are separated by the plane $\mathcal{P}$ (see Subsection 4). We will choose $\mathcal{P}$ perpendicular to the x-axis at $x = L/2$. Thus, Property 2 will guarantee that the whole AFM lie in the maneuvering region whenever the end-effector lies in the maneuvering region (and $\theta_0 = \varphi = 0$).

Property 3: *Let $b = 0$. Let $a_2 = 0$, $\theta_0 = 0$, and $\varphi = 0$. Let $x(s)$ demote the x-coordinate* *of* $\mathbf{r}(s)$*. If* $x(L) > L/3$*, then autocollision cannot occur.*

The condition $b = 0$ occurs when the end-effector is in the plane $z = 0$. Then the whole AFM is also contained in the plane $z = 0$. As mentioned in Subsection 5.1, autocollision may occur. Property 3 will be used to make sure autocollision cannot happen.

7 Generation of π_1

We now describe Step 2 of the planning approach outlined in Subsection 4. We apply the above results to the generation of the path π_1 in the maneuvering region $\mathcal{W}_0$.

We will enforce the condition $\theta_0 = \varphi = 0$ throughout π_1, so that Properties 1 and 2 will apply. We restrict the motion of the end-effector to the half-space $y \geq 0$ as suggested by Property 1. We also choose $\mathcal{P}$ perpendicular to the x- axis of the coordinate system at the abscissa $x = L/2$, as suggested by Property 2.

The inputs to Step 2 are the initial configuration $\mathbf{r}_I(.)$ of the AFM and the intermediate configuration $(\mathbf{r}_\mathcal{P}, \mathbf{T}_\mathcal{P})$ of its end-effector. The curve $\mathbf{r}_I(.)$ is assumed[3] to be a helix-like curve verifying $\theta_0 = \varphi = 0$, lying in $\mathcal{W}_0 \cap \{y \geq 0\}$, and with the end-effector in the reachable volume $\mathcal{V}$ defined in Subsection 5.3. The point $\mathbf{r}_\mathcal{P}$ is in $\mathcal{P} \cap \mathcal{V}$. In Section 8 we will compute $\mathbf{r}_\mathcal{P}$ to satisfy this condition.

We let $\mathbf{r}[\xi](.)$ designate the helix-like AFM's configuration defined by the state vector ξ. Formally, the path π_1 is a continuous map:

$$\pi_1 : u \in [0,1] \mapsto \xi(u) \in \mathbf{R}^5,$$

such that:
- $\mathbf{r}[\xi(0)](.) = \mathbf{r}_I(.)$, $\mathbf{r}[\xi(1)](L) = \mathbf{r}_\mathcal{P}$ and $(\mathbf{r}[\xi(1)])'(L) = \mathbf{T}_\mathcal{P}$,
- for every $u \in [0,1]$, $\mathbf{r}[\xi(u)](.)$ is fully contained in $\mathcal{W}_0$ and the θ_0 and φ components of $\xi(u)$ are identically null.

Let z_I and $z_\mathcal{P}$ denote the z coordinate of $\mathbf{r}_I(L)$ and $\mathbf{r}_\mathcal{P}$, respectively. Let us first assume that z_I and $z_\mathcal{P}$ are both positive, or both negative. Since $\mathcal{V}$ is convex the line segment joining $\mathbf{r}_I(L)$ to $\mathbf{r}_\mathcal{P}$ lies in $\mathcal{V}$. The path π_1 is computed by translating the end-effector along this line segment and letting the intermediate helix-like configurations be defined by the inverse kinematic equations with $\theta_0 = \varphi = 0$ (Equ. (27) through (29)). Properties 1 and 2 guarantee that all intermediate configurations lie in $\mathcal{W}_0 \cap \{y \geq 0\}$.

If z_I and $z_\mathcal{P}$ have different signs, then the end- effector traverses the plane $z = 0$, where $b = 0$ and autocollision may occur. To prevent autocollision we make use of Property 3. In fact, we need Property 3 extended to the case where $a_2 \neq 0$, which we have not been able to prove analytically. The case where $a_2 = 0$, which corresponds to the situation where the end-effector lies in the x-axis ($y = 0$), seems to be the worst-case situation regarding autocollision. To be complete, however, we have made a systematic numerical analysis in the case where $a_2 \neq 0$, which actually shows that autocollision does not occur when the x coordinate of the end-effector is greater than $L/3$. Therefore, if the segment joining $\mathbf{r}_I(L)$

[3] This assumption is not very restrictive since the planner can always find a way to bring back the robot to such a configuration. At the very beginning one can achieve such a configuration, for example by removing all obstacles.

to $\mathbf{r}_\mathcal{P}$ intersects the plane $z = 0$ at a point whose abscissa is greater than $L/3$, autocollision does not occur, and we proceed as in the case described above where z_I and $z_\mathcal{P}$ had the same sign. If the abscissa of the intersection point is less than or equal to $L/3$, we introduce an intermediate point at an abscissa $L/3 + \varepsilon$, with $\varepsilon > 0$, in the plane $z = 0$. We then translate the end-effector from its initial position to this intermediate point and next from this point to the final position.

If $z_\mathcal{P} = 0$, we proceed as if it had the same sign as z_I, since the x coordinate of $\mathbf{r}_\mathcal{P}$ is $L/2 > L/3$. Whenever $z_I = 0$, we assume that the x coordinate of $\mathbf{r}_I(L)$ is greater than $L/3$, so that we can proceed as in the case where z_I and $z_\mathcal{P}$ have the same sign.

In the following we let $\mathbf{r}_\mathcal{P}(.)$ denote the configuration of the AFM attained at the end of path π_1. It is completely determined by the intermediate configuration $(\mathbf{r}_\mathcal{P}, \mathbf{T}_\mathcal{P})$ of the end-effector and by the fact that the AFM has a helix-like shape with $\theta_0 = \varphi = 0$.

8 Generation of μ

We now describe Step 1 of the planning method. The goal is to generate a smooth collision-free curve $\mu : [0, 1] \rightarrow \mathbf{R}^3$ connecting a point $\mathbf{r}_\mathcal{P} \in \mathcal{P}$ to the desired goal position $\mathbf{r}_G$ of the end-effector. Hence, $\mu(0) = \mathbf{r}_\mathcal{P}$ and $\mu(1) = \mathbf{r}_G$.

The curve μ should satisfy various properties. The point $\mathbf{r}_\mathcal{P}$ must be in $\mathcal{V}$ (see Subsection 5.3). The unit vector $\mathbf{T}_\mathcal{P}$ pointing along the tangent to μ at $\mathbf{r}_\mathcal{P}$ must be equal to $(\sqrt{1-b^2}, 0, b)$, so that the state parameters θ_0 and φ be null when the end-effector is located at $\mathbf{r}_\mathcal{P}$ with orientation $\mathbf{T}_\mathcal{P}$ (see Equ. 7 and 13). At the other endpoint of μ, the tangent vector $\mu'(1)$ should point along the desired goal orientation $\mathbf{T}_G$ of the end-effector. Finally, there should exist a configuration of the AFM whose subset contained in $\mathcal{W}_1$ coincides with μ, while the rest (contained in $\mathcal{W}_0$) is a helix-like curve of length $L - d$ (with d being the length of μ).

We construct μ as follows. Let $\mathcal{S}$ be the ball of radius L centered at the origin. We first decompose the volume $\mathcal{S} \cap \mathcal{W}_1$ into an array of cubic cells. We then search for a sequence of adjacent cells, called a *channel*, having no intersection with the obstacles, such that the first cell has one face contained in $\mathcal{P}$ with non-empty intersection with $\mathcal{V}$ and the last cell contains $\mathbf{r}_G$. We finally construct μ as a sequence of B-spline curves lying in the channel.

Channel Generation: We generate a channel using a simple variant of a classical path planning approach known as the "approximate cell decomposition" approach [14]. We enclose $\mathcal{S} \cap \mathcal{W}_1$ in a cube parallel to the coordinate axes and decompose into an array of cubic cells of constant size. Every cell fully contained in $\mathcal{S}$ with no intersection with the obstacles is said to be empty. A graph G representing adjacency among the empty cells is constructed. The cells of G that have one face $\mathcal{P}$ with a non-empty intersection with $\mathcal{V}$ are called the *initial cells*. The cell of G that contains $\mathbf{r}_G$, if any, is called the *goal cell*. The graph is then searched for a path connecting an initial cell (anyone) to the goal cell. If such a path is found, it defines a channel.

There exist more efficient approximate cell decomposition techniques generating parallelepipedic cells of various sizes (*e.g.*, see [21]). However, generating cubic cells of equal dimension simplify the construction of the B-spline curves, as described below.

Trajectory Generation: Let the constructed channel be $\mathcal{K} = (\kappa_1, \kappa_2, ..., \kappa_N)$, where κ_1 is an initial cell and κ_N is the goal cell. Every two consecutive cells in $\mathcal{K}$ are adjacent, *i.e.* share one face. Our goal is to generate a smooth curve in $\mathcal{K}$ connecting a point of $\kappa_1 \cap \mathcal{P} \cap \mathcal{V}$ to $\mathbf{r}_G$. We generate this curve as a sequence of B-spline curve segments computed using control points contained in $\mathcal{K}$. The interesting property of a B-spline curve segment is that it is fully contained in the convex hull of the control points used to compute it. We use this property to choose the control points in the channel $\mathcal{K}$ so that the generated curve is guaranteed to also lie in $\mathcal{K}$. (B-spline approximation techniques have already been used in path planning to extract smooth paths from two-dimensional channels [20].)

We recall that a B-spline of degree m is a curve whose point coordinates are polynomials of degree m of some parameter t. The coefficients of the polynomials are completely determined by the coordinates of $m+1$ *control points*. The choice of the degree m is determined by how smooth we want the junction between two successive curve segments to be. If the derivatives have to be continuous up to the order k, then we should use B-splines of degree $k+1$. In our case, we want to generate a curve that will be tracked by the AFM, hence requiring that the curvature and the torsion of the curve be continuous. Since the curvature and the torsion involve the computation of derivatives of orders 2 and 3, respectively, we must use B-splines of degree 4, also called *quadric splines*. A quadric spline curve with $q+1$ ($q \geq 4$) control points $\mathbf{c}_0, \mathbf{c}_1, ..., \mathbf{c}_q$ is formed by $q-3$ curve segments $\mathbf{p}_i(t)$ defined by:

$$\mathbf{p}_i(t) = X_0(t)\mathbf{c}_{i-1} + X_1(t)\mathbf{c}_i + X_2(t)\mathbf{c}_{i+1} + X_3(t)\mathbf{c}_{i+2} + X_4(t)\mathbf{c}_{i+3}, \tag{33}$$

where $i = 1, ..., q-3$ and $X_0(t), X_1(t), X_2(t), X_3(t)$ and $X_4(t)$ are the *quadric polynomial basis functions* of degree 4 in the parameter $t \in [0, 1]$. Any two consecutive curve segments $\mathbf{p}_i(t)$ and $\mathbf{p}_{i+1}(t)$ join together at the point $\mathbf{p}_i(1) = \mathbf{p}_{i+1}(0)$ with continuous derivatives up to order 3.

Let $\mathbf{M}$ be the matrix of coefficients of the quadric polynomials, also called *B-spline basis matrix*. It is defined as:

$$\mathbf{M} = \frac{1}{24}\begin{pmatrix} 1 & -4 & 6 & -4 & 1 \\ -4 & 12 & -12 & 4 & 0 \\ 6 & -6 & -6 & 6 & 0 \\ -4 & -12 & 12 & 4 & 0 \\ 1 & 11 & 11 & 1 & 0 \end{pmatrix} \tag{34}$$

Posing:

$$\mathbf{G}_i = (\mathbf{c}_{i-1} \cdots \mathbf{c}_{i+3})^T, \tag{35}$$

we can rewrite Equ. (33) as:

$$\mathbf{p}_i(t) = [t^4, t^3, t^2, t, 1]\, \mathbf{M}\, \mathbf{G}_i. \tag{36}$$

Each segment $\mathbf{p}_i(t)$ approximates the shape of the polygonal line connecting its control points, but in general they do not interpolate the control points $\mathbf{c}_{i-1}$ through $\mathbf{c}_{i+3}$. The curve can be forced to traverse any specific control point by repeating it. A desired orientation can be achieved at this point by selecting the two adjacent control points in the line passing through this point and parallel to this orientation. Hence, we can build a curve whose endpoints are exactly $\mathbf{r}_{\mathcal{P}}$ and $\mathbf{r}_G$, with the appropriate orientations $\mathbf{T}_{\mathcal{P}}$ and $\mathbf{T}_G$.

Positioning the Control Points: The generation of μ within the channel $\mathcal{K}$ is now reduced to the selection of a sequence of control points $\mathbf{c}_0$, $\mathbf{c}_1$, ..., so that the convex hull of every five consecutive points lies within the channel. Since all cells are cubes, hence are convex, the B-spline generated by successive control points contained in the same cell κ_i lies entirely in κ_i. The problem arises only when the B-spline is generated using control points in different cells.

Let F_i denote the common face of two successive cells κ_{i-1} and κ_i in $\mathcal{K}$. We say that κ_i is a *no-corner cell* if the faces F_i and F_{i+1} are parallel, and a *cornel cell* otherwise. Assume that the channel $\mathcal{K}$ contains at least one corner cell (if this is not the case, the problem of generating a curve in the channel is trivial). The control points are selected only in the initial, goal and corner cells. For every corner cell, call it κ_i, we proceed as follows. Let $\mathbf{m}_i$ and $\mathbf{m}_{i+1}$ be the midpoints of the faces F_i and $F_{i+1}$of κ_i. The following four aligned control points are selected in κ_i:

$$\mathbf{m}_i, \quad \mathbf{m}_i + \frac{1}{3}(\mathbf{m}_{i+1} - \mathbf{m}_i), \quad \mathbf{m}_i + \frac{2}{3}(\mathbf{m}_{i+1} - \mathbf{m}_i), \quad \text{and} \quad \mathbf{m}_{i+1}.$$

In the initial (resp. goal) cell, we generate five control points to generate a curve that starts $\mathbf{r}_{\mathcal{P}}$ (resp. finishes at $\mathbf{r}_G$) with the desired orientations. The point $\mathbf{r}_{\mathcal{P}}$ (repeated control point) is selected as the center of the face F_1, with $\mathbf{T}_{\mathcal{P}} = (\sqrt{1-b^2}, 0, b)$ and $b = z_{\mathcal{P}}/L$ (Equ. 27).

Let us now consider a continuous subset of the channel, say $\kappa_k, ., \kappa_{k+l}$, with $l \geq 1$, such that κ_k is either the initial cell or a corner cell, κ_{k+l} is either the goal cell or a corner cell, and $\kappa_{k+1}, ..., \kappa_{k+l-1}$ are all no-corner cells. We call such a subset of $\mathcal{K}$ a *line-subchannel.* Each line-subchannel in $\mathcal{K}$ contains 8, 9, or 10 control points. One can easily verify that the convex-hull of any five consecutive control points lies in the line-subchannel.

Feasibility Check: The concatenation of the B-spline curve segments generated using the control points generated as above forms a smooth collision-free curve joining $\mathbf{r}_{\mathcal{P}}$ to $\mathbf{r}_G$. Let d be the length of this curve. The inverse kinematics equations of Subsection 5.3 are used to verify that the end-effector of an AFM of length $L - d$ can achieve the configuration $(\mathbf{r}_{\mathcal{P}}, \mathbf{T}_{\mathcal{P}})$. If it cannot, one may attempt to generate another curve μ, for instance by generating a different channel.

9 Generation of π_2

The goal of Step 3 is to generate a path π_2 connecting intermediate configuration $\mathbf{r}_{\mathcal{P}}(.)$ to a goal configuration where the end-effector is at $(\mathbf{r}_G, \mathbf{T}_G)$. Our approach consists of making the end-effector track μ in the working region, until it reaches its goal $\mathbf{r}_G$, with the rest of AFM following it along the same path. The portion of the AFM in the maneuvering region keeps a helix-like shape (of length less than L) computed using the inverse kinematic equations of Subsection 5.3.

Hence, we build π_2 as the continuous map:

$$\pi_2 : u \in [0, d] \mapsto \mathbf{r}(u, .) = \mathbf{r}_u(.) \in \mathcal{C}_L,$$

with $\mathbf{r}_0(.) = \mathbf{r}_{\mathcal{P}}(.)$. For every $u \in [0, d]$ (d is the length of μ), $\mathbf{r}_u(.)$ is the concatenation of the following two curves:

- the helix-like curve of length $L-u$ lying in $\mathcal{W}_0$ and such that $\mathbf{r}_u(L-u) = \mathbf{r}_\mathcal{P}$ and $\mathbf{r}'_u(L-u) = \mathbf{T}_\mathcal{P}$;
- the portion of μ of length u joining $\mathbf{r}_\mathcal{P}$ to $\mathbf{r}_u(L)$ and entirely contained in $\mathcal{W}_1$.

One important remark should be made here. The AFM has five state parameters a_1, a_2, b, θ_0, and φ. For a given length of the AFM, the parameters a_1 and a_2 determine the x and y coordinates of the end-effector, and the parameter b determines its z coordinate. The intermediate end-effector's configuration $(\mathbf{r}_\mathcal{P}, \mathbf{T}_\mathcal{P})$ has been computed such that, when the end-effector of an helix-like AFM of length L is at this configuration, the parameters θ_0 and φ are null. Along the path π_2, the length of the portion of the AFM in $\mathcal{W}_0$ is $L-u$, with $u \in [0, d]$. While this length varies, we need to adjust b and φ (θ_0 remains null). We must show that the rotation about the y-axis caused by the variation of φ does not lead the portion of the AFM of length $L-u$ to enter the working region where it could collide with obstacles. Indeed, Property 2 guarantees us that it stays in the maneuvering region only when θ_0 and φ are null. For non-zero values of any of these angles, the property is much more complicated to establish analytically. Instead, we ran a systematic numerical analysis by positioning the end-effector of an AFM of length L at the points of a fine grid defined in the intersection of the reachable volume $\mathcal{V}$ and the plane $\mathcal{P}$, and by rotating the end-effector at each point of this grid. This analysis shows that the AFM stays in the maneuvering region.

10 Implementation and Experimentation

We implemented the techniques presented above in an interactive path planner written in the C language and running on a Silicon Graphics Personal IRIS Workstation. The generated paths are displayed using the simulated AFM shown in Figure 1.

Figure 2 shows a typical path illustrating the planning method described in the previous three sections.

Figure 6 displays graphic scenes generated in the context of a simple pipe manipulation problem. The AFM operates in a workspace containing cylindrical pipes and parallelepipedic obstacles, as illustrated in Figure 6.*a*. The goal is to remove the pipes and stack them on the side. Figures 6.*b* and 6.*c* display instances of the AFM manipulating pipes. To run this example, we have added a simple technique to the planner for deciding which pipe is to be removed next. We also make the simplifying assumptions that each pipe can only be translated and that it is originally parallel to the x or the z-axis of the coordinate system.

The planner is fast enough to be run on-line without significantly slowing down graphic animation.

The graphic rendering of the AFM is done by sweeping a disc perpendicular to the AFM spine. The spine consists of two portions, the helix-like portion (possibly the entire spine), and the spline portion (possibly of zero length). Along the helix-like portion, the plane containing the swept disc is defined by the normal $\mathbf{N}$ and binormal $\mathbf{B}$ calculated using the following expressions:

$$\mathbf{N}(s) = (-\sin\theta(s),\ \cos\theta(s),\ 0), \tag{37}$$

$$\mathbf{B}(s) = (-b\ \cos\theta(s), -b\ \sin\theta(s),\ a). \tag{38}$$

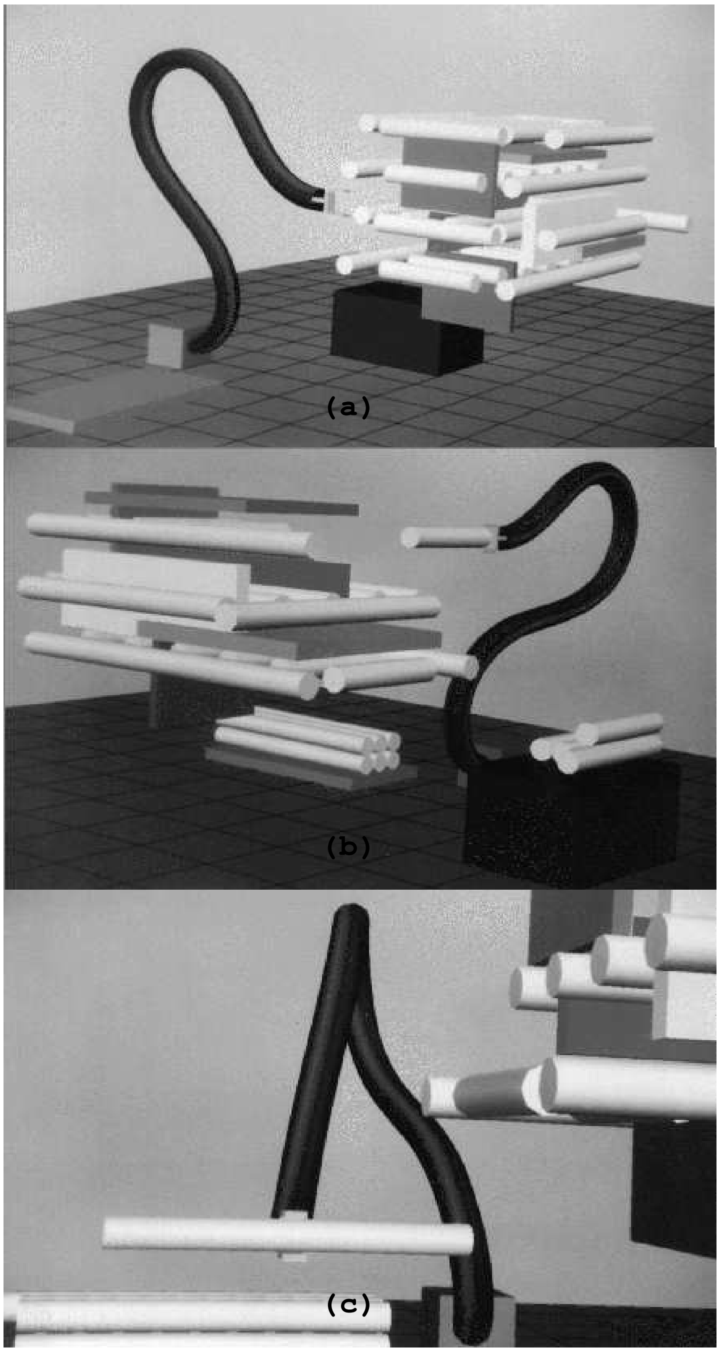

Figure 6: Pipe manipulation

Along the spline portion, the normal $\mathbf{N}$ and binormal $\mathbf{B}$ are computed using the expressions of the first and second derivatives of a B-spline curve segment $\mathbf{p}_i$:

$$\mathbf{p}_i'(t) = [4t^3, 3t^2, 2t, 1, 0]\,\mathbf{M}\ \mathbf{G}_i. \tag{39}$$

$$\mathbf{p}_i''(t) = [12t^2, 6t, 2, 0, 0]\,\mathbf{M}\ \mathbf{G}_i. \tag{40}$$

The spine is approximated as a sequence of straight line between a finite number of points $\mathbf{r}_i$, $i = 1, ..., \ell$ ($\ell = 60$ in the figures shown in this paper). At each point $\mathbf{r}_i$ the swept disc is approximated as a m-sided polygon whose vertices are $\mathbf{v}_{ij} = \mathbf{N}(s_i)\cos\omega_j + \mathbf{B}(s_i)\sin\omega_j$, with $\omega_j = 2\pi j/m$ and $j \in [0, m-1]$. The AFM manipulator is then displayed as a collection of adjacent triangular meshes which are rendered using the drawing subroutines available in the graphic library of the workstation.

11 Conclusion

We have presented an efficient path planning approach to generate the collision-free paths of an actively flexible manipulator of constant length among stationary obstacles in a three-dimensional workspace. The approach consists of planning the path of the end-effector and letting the rest of the AFM follow this path. The main problem is to manage the bent curve between the AFM's fixed end to its entry in the end-effector's path. To that purpose we partition the workspace into an empty maneuvering region containing that bent curve and a working region containing all the obstacles and the end-effector's path. The portion of the AFM in the maneuvering region is managed by giving it a convenient helix- like shape. The planning of a collision-free path for the end-effector in the working region is done by combining a simple variant of the well-known approximate cell decomposition approach and B- spline approximation techniques. The notion of helix-like curve was not previously used in robotics to control flexible manipulators. Its nice geometrical properties and the fact that it yields closed-form inverse kinematic expressions make it extremely suitable for such manipulators.

Throughout this paper we only considered the application of our techniques to robotic automation. However, there has recently been an increase of interest among the computer graphics community in producing animated sequences of images with deformable objects (*e.g.*, [18, 19, 16, 17]). We think that the work presented above could be applied to this area for reducing the amount of input data necessary to generate such sequences.

References

[1] G. S. Chirikjian and J. W. Burdick, A Modal Approach to the Kinematics of Hyper-Redundant Manipulators, Robotics and Mechanical Systems Report No. RMS-89-3, Dept. of Mechanical Engineering, California Institute of Technology, Sept. (1989).

[2] G. S. Chirikjian and J. W. Burdick, An Obstacle Avoidance Algorithm for Hyper-Redundant Manipulators. IEEE Robotics and Automation, Vol. 1, 625, (1990).

[3] W.I. Clement and R.M. Iñigo, Design of a Snake- Like Manipulator. Robotics and Autonomous Systems, Vol. 6, 265-282 (1990).

[4] J.J. Craig, Introduction to Robotics. Mechanics and Control, Addison-Wesley, Reading, MA, 1986.

[5] M. Ivanescu and I. Badea, Dynamic Control for a Tentacle Manipulator, Int. Conf. on Robotics and Factories of the Future, pp. 317-328, Charlote, Nc, USA, (1984).

[6] W.K. Taylor, D. Lavie and I.I. Esat, A Curvilinear Snake Arm Robot with Gripper-Axis Fibre-Optic Image Processor Feedback, Robotica, Vol. 1, 33-39 (1983).

[7] M.M. Lipschutz, Differential Geometry, Schaum's Outline Series in Mathematics, McGraw-Hill Book Company, New York, (1969).

[8] D. Steward, A Platform with six degrees of freedom. Proc. Inst. Mech. Engr., Vol. 180, Pt 1 No. 15, 371-386, (1965).

[9] K. Suzumori, S. Iikura, and H. Tanaka, Development of Flexible Microactuator and Its Applications to Robotic Mechanisms, Proceedings of the 1991 IEEE International Conference on Robotics Automation, Sacramento, CA, 1622-1627, (1991).

[10] K. Oosting and S.L. Dickerson, Simulation of a High Speed Light Weight Arm, IEEE Int. Conf. Robotics and Automation, Philadelphia, PA, pp. 494-496, (1988).

[11] H.G. Lee, F. Miyazaki, and S. Arimoto, Liapunov Stability Analysis for PDS control of Flexible Multi-Link Manipulator, Proc. of 27'th IEEE CDC, Vol. 1 75-80, (1988).

[12] Jr.R.H. Cannon, and E. Schmitz,Initial Experiments on the End Point Control of a Flexible One-link Robot, Int. J. of Robotics, Vol. 3, No. 3, 499-502, (1984).

[13] H.G. Lee, H. Kanoh, S. Kawamura, and F. Miyazaki, Stability Analysis of One-link Flexible Arm Control by a Linear Feedback Laws, Proc. of IMACS/IFAC Int. of Symposium DSP. 277-284, (1987).

[14] J. C. Latombe, Robot Motion Planning, Kluwer Academic Publishers, Boston, (1991).

[15] J. Barraquand, and J. C. Latombe, Robot Motion Planning: A Distributed Representation Approach, Technical Report STAN- CS-89-1257, Department of Computer Science, Stanford University, May., (1989).

[16] Badler, Manoochehri, Walters, Articulated Figure Positioning by Multiple Constraints, IEEE CG&A, June 1987.

[17] J. Wilhelms, Using Dynamic Analysis for Realistic Animation of Articulated Bodies, IEEE CG&A, June, 1987.

[18] D. Terzopoulos, J.C. Platt, A.H. Barr, and K. Fleisher, Elastically Deformable Models, SIGGRAPH 87, 205-214, (1987).

[19] J.C. Platt and A.H. Barr, Constraint Methods for flexible Models, SIGGRAPH 88, 279-288, (1988).

[20] K. Kant, S.W. Zucker , Planning Smooth Collision- Free Trajectories: Path, Velocity and Splines in Free-Space.

[21] D. Zhu and J.C. Latombe, New Heuristic Algorithms for Efficient Hierarchical Path Planning, IEEE Transactions on Robotics and Automation, 7(1), 9-20 (1991).

[22] M. Abramowitz and I. Stegus, *Handbook of Mathematical Functions*, Dover.

Appendices

Throughout the following appendices we consider an AFM of length L with a helix-like shape, as defined in Section 3.

A. Simplification of the Direct Kinematics Computation

Let $\theta_0 = 0$ and $\varphi = 0$. Equ. (13) implies that $\theta(s) + \theta(s + L/2) = a_2 L/\pi$, for all $s \in [0, L/2]$. Using Equ. (9) and denoting the x, y, and z coordinates of $\mathbf{r}(s)$ by $x(s)$, $y(s)$, and $z(s)$, we get:

$$x(s + L/2) = x(L/2) + \cos(\frac{a_2 L}{\pi})\, x(s) + \sin(\frac{a_2 L}{\pi})\, y(s), \tag{41}$$

$$y(s + L/2) = y(L/2) + \sin(\frac{a_2 L}{\pi})\, x(s) - \cos(\frac{a_2 L}{\pi})\, y(s), \tag{42}$$

$$z(s + L/2) = z(L/2) + z(s). \tag{43}$$

These equations remain valid when $\theta_0 \neq 0$ and $\varphi \neq 0$, since changes in the values of θ_0 and φ only cause rigid-body displacements of the AFM. They cut the direct kinematics computation by one half. Their geometrical interpretation is that the second half of the AFM's spine can be generated by successively applying a translation, a rotation and a reflexion to the first half of the spine.

A direct consequence of Equ. (41) and (42) is that:

$$||\mathbf{r}(s)|| = ||\mathbf{r}(s + L/2) - \mathbf{r}(L/2)||. \tag{44}$$

Taking $s = L/2$, we obtain that the Euclidean distance between the fixed end $\mathbf{r}(0)$ and the midpoint $\mathbf{r}(L/2)$ of the AFM is the same that the distance between $\mathbf{r}(L/2)$ and the end-effector $\mathbf{r}(L)$.

B. Inverse Kinematics of a Helix-Like AFM

The direct kinematic equations (14) and (15) yield:

$$c_1 = a\, \cos\varphi\, \cos\theta_0 + b\, \sin\varphi \tag{45}$$

$$c_2 = a\, \sin\theta_0 \tag{46}$$

$$c_3 = -a\, \sin\varphi\, \cos\theta_0 + b\, \cos\varphi \tag{47}$$

$$x = a\, \cos\varphi\, (\tilde{x}\, \cos\theta_0 - \tilde{y}\, \sin\theta_0) + L\, b\, \sin\varphi \tag{48}$$

$$y = a\, \tilde{x}\, \sin\theta_0 + a\, \tilde{y}\, \cos\theta_0 \tag{49}$$

$$z = -a\, \sin\varphi\, (\tilde{x}\, \cos\theta_0 - \tilde{y}\, \sin\theta_0) + L\, b\, \cos\varphi. \tag{50}$$

Due to the relation $c_1^2 + c_2^2 + c_3^2 = 1$, these equations reduce to 5 independent equations in the 5 unknowns a_1, a_2, b, θ_0, and φ.

Multiplying Equ. (45) and (47) by $\sin\varphi$ and $\cos\varphi$, respectively, we obtain:

$$b = c_1\, \sin\varphi + c_3\, \cos\varphi. \tag{51}$$

Similarly, from Equ. (48) and (50), we get:

$$L\ b = x\ \sin\varphi + z\ \cos\varphi. \tag{52}$$

¿From (51) and (52), we obtain the expression for the angle φ:

$$\varphi = \arctan\frac{z - L\ c_3}{L\ c_1 - x}. \tag{53}$$

Then, the parameter b is directly given by (51).
The angle θ_0 is derived using Equ. (46):

$$\theta_0 = \arcsin(c_2/a). \tag{54}$$

Since the length of a vector remains constant under orthonormal transformations, the matricial expression (14) yields:

$$x^2 + y^2 + z^2 = a^2\tilde{x}^2 + a^2\tilde{y}^2 + L^2b^2. \tag{55}$$

Using the definitions of the quantities $\tilde{x}$ and $\tilde{y}$ given in Equ. (16) and (17), we can write:

$$\tilde{x}^2 + \tilde{y}^2 = L^2J_0^2(\frac{L}{2\pi}\sqrt{a_1^2 + a_2^2}) \tag{56}$$

Substituting (56) into (55) and rearranging, we get:

$$J_0(\frac{L}{2\pi}\sqrt{a_1^2 + a_2^2}) = \sqrt{\frac{x^2 + y^2 + z^2 - (Lb)^2}{(La)^2}}. \tag{57}$$

Equ. (16), (17), and (49) yield:

$$y = a\ L\ \sin(\theta_0 + \frac{a_2L}{2\pi})\ J_0(\frac{L}{2\pi}\sqrt{a_1^2 + a_2^2}). \tag{58}$$

Thus, a_2 can be calculated by combining Equ. (57) and (58). Equ. (57) then yields the expression of a_1. We get:

$$a_2 = \frac{2\pi}{L}\ \arcsin\frac{y}{\sqrt{x^2 + y^2 + z^2 - (Lb)^2}} - \frac{2\pi}{L}\ \theta_0. \tag{59}$$

$$a_1 = \pm\sqrt{\left(\frac{2\pi}{L}\right)^2\left(J_0^{-1}(\sqrt{\frac{x^2 + y^2 + z^2 - (Lb)^2}{(La)^2}})\right)^2 - a_2^2}. \tag{60}$$

C. Inflection Points of the AFM

Let $\theta_0 = 0$ and $\varphi = 0$. From Equ. (11) we see that the sign of the curvature of the AFM changes at points whose arc-lengths s_1 and s_2 are solutions of $\tan(2\pi s/L) = -a_1/a_2$. Posing $\alpha = \arctan a_2/a_1$, we see that there exist at most two solutions s_1 and s_2 defined by:

$$s_1 = L/4 + L\alpha/2\pi \quad \text{and} \quad s_2 - s_1 = L/2, \tag{61}$$

which are comprised between 0 and L. Hence, the AFM has a maximum of two inflection points of arc-length s_1 and s_2, respectively.

In the particular case where $a_2 = 0$, we have $\alpha = 0$, $s_1 = L/4$ and $s_2 = 3L/4$. Then (see [22] pp. 498-499):

$$x(s_1) = a\int_0^{L/4} \cos(\frac{a_1 L}{2\pi}\sin\frac{2\pi s}{L})\,ds = a\frac{L}{4}J_0(\frac{a_1 L}{2\pi}) = \frac{x(L)}{4}, \tag{62}$$

$$x(\frac{L}{2}) = a\int_0^{L/2} \cos(\frac{a_1 L}{2\pi}\sin\frac{2\pi s}{L})\,ds = a\frac{L}{2}J_0(\frac{a_1 L}{2\pi}) = \frac{x(L)}{2}. \tag{63}$$

¿From Equ. (41) and the above relations we derive:

$$x(s_2) = \frac{3x(L)}{4}. \tag{64}$$

A similar calculation yields:

$$y(s_2) = y(s_1) = a\frac{L}{4}H_0(\frac{La_1}{2\pi}) \tag{65}$$

and

$$y(L/2) = a\frac{L}{2}H_0(\frac{La_1}{2\pi}), \tag{66}$$

where the function H_0 is the Struve function of zero degree [22]. If $a_1 = 0$, then $\alpha = \pi/2$, $s_1 = L/2$ and $s_2 = L$. The AFM has a single inflection point.

D. Proof of Property 1

Property 1: *Let $\theta_0 = 0$. Let $y(s)$ denote the y coordinate of $\mathbf{r}(s)$. If $y(L) \geq 0$, then $y(s) \geq 0$ for all $s \in [0, 1]$.*

Proof: From Equ. (13) we derive that $\theta(s) = 0$ at $s = 0, L/2 + L2\alpha/2\pi$, and L, where $\alpha = \arctan a_2/a_1$ (see Appendix C), and that $\theta'(s) = 0$ at $s = L/4 + L\alpha/2\pi$ and $3L/4 + L\alpha/2\pi$ (the inflection points, if they exist).

When $s \in (0, L/2 + 2L\alpha/2\pi)$, we have $\theta(s) \in (0, \pi)$. Hence, $y(s)$ increases monotonically (see Equ. (9)) and is greater than or equal to 0.

When $s \in (L/2 + 2L\alpha/2\pi, L)$, we have $\theta(s) \in (-\pi, 0)$. Hence, $y(s)$ decreases monotonically. Since it is greater than or equal to 0 at both ends, it is greater than or equal to 0 in the whole interval.

If $a_1 = 0$, then $\alpha = \pi/2$ and $y(s)$ increases monotonically along the whole AFM. □

E. Extrema of the Function $x(s)$

Let $x(s)$ and $y(s)$ denote the x and y coordinates of $\mathbf{r}(s)$. We now analyze the extrema of $x(s)$ when $\theta_0 = \varphi = 0$ and $y(L) \geq 0$. The results of this analysis will be used in the next appendix to prove Property 2.

The arc-lengths s_{max} where $x(s)$ is locally maximal satisfy $x'(s_{max}) = 0$ and $x''(s_{max}) < 0$. The arc-lengths s_{min} where $x(s)$ is locally minimal satisfy $x'(s_{min}) = 0$ and $x''(s_{min}) > 0$.

The equation $x'(s) = 0$ implies that $\theta(s) = \pm\pi/2$. Several cases arise which depend on the values of a_1 and a_2.

1. The function $x(s)$ has no local extrema.

2. The function $x(s)$ has only a local maximum $s^{(1)}_{max}$ and a local minimum $s^{(1)}_{min}$.

3. The function $x(s)$ has two local maximum, $s^{(1)}_{max}$ and $s^{(2)}_{max}$, and two local minimum, $s^{(1)}_{min}$ and $s^{(2)}_{min}$.

The case 1 ocurrs when the equations $\theta(s) = \pm\pi/2$ has no real solutions or these are such that $x''(s) = 0$. It corresponds to values of a_1 and a_2 satisfying $\pi^2/L - a_2 \geq \sqrt{a_1^2 + a_2^2}$. The function $x(s)$ attains its absolute minimum and maximum at the endpoints $s = 0$ and $s = L$, respectively. The case $\pi^2/L - a_2 = \sqrt{a_1^2 + a_2^2}$ corresponds to an inflection point s_1.

The case 2 ocurrs when the equation $\theta(s) = \pi/2$ has real solutions with $x''(s) \neq 0$ but the equation $\theta(s) = -\pi/2$ has no real solutions or these are such that $x''(s) = 0$. It corresponds to values of a_1 and a_2 satisfying $\pi^2/L + a_2 \geq \sqrt{a_1^2 + a_2^2} > \pi^2/L - a_2$. The case $\pi^2/L + a_2 = \sqrt{a_1^2 + a_2^2}$ corresponds to a second inflection point s_2.

The case 3 ocurrs when both equations $\theta(s) = \pm\pi/2$ have real solutions with $x''(s) \neq 0$. It corresponds to values of a_1 and a_2 satisfying $\sqrt{a_1^2 + a_2^2} > \pi^2/L + a_2$.

The solutions of $\theta(s) = \pi/2$ are given by $s = (L/2\pi)(\alpha + \sigma_1)$, with $\alpha = \arctan a_2/a_1$ (see Appendix C) and:

$$\sin\sigma_1 = \frac{2\pi}{L\sqrt{a_1^2 + a_2^2}}\left(\frac{\pi}{2} - \frac{a_2 L}{2\pi}\right). \tag{67}$$

We recall that $a_1 \geq 0$ and $a_2 \geq 0$ (since $y(L) \geq 0$). Let us assume that they are not null simultaneously. Then $0 \leq \alpha \leq \pi/2$. In addition, since we only consider positive or null x and y coordinates of the end-effector, we have $0 \leq \pi/2 - (a_2 L)/(2\pi)$, with $a > 0$ (see Equ. (18) and (19)). Therefore, $\sigma_1 \in [0, \pi]$. If $\sigma_1 = \pi/2$, the point of arc-length $s = (L/2\pi)(\alpha + \sigma_1)$ is an inflection point of the AFM, not a local maximum. If $\sigma_1 \neq \pi/2$, Equ. (67) admits two distinct solutions. One can verify that the solution with $\sigma_1 \in [0, \pi/2)$ corresponds to a local maximum $s^{(1)}_{max}$, while the solution with $\sigma_1 \in (\pi/2, \pi]$ corresponds to a local minimum $s^{(1)}_{min}$. At the local maximum, we have $\alpha + \sigma_1 < \pi$. Therefore, $0 < s^{(1)}_{max} < L/2$. Since $x(s^{(1)}_{max}) \leq s^{(1)}_{max}$, we conclude that the first local maximum is less than or equal to $L/2$.

The equation $\theta(s) = -\pi/2$ can yield a second local maximum (and minimum). It admits real solutions when a_1 and a_2 verify $\pi^2/L + a_2 \leq ({a_1}^2 + {a_2}^2)^{1/2}$. We let $\mathcal{N}$ denote the set of values (a_1, a_2) defined by this constraint. When $(a_1, a_2) \in \mathcal{N}$, the solutions are given by $s = (L/2\pi)(\alpha + \sigma_2)$, with α defined as above and σ_2 solution of:

$$\sin\sigma_2 = \frac{2\pi}{L\sqrt{a_1^2 + a_2^2}}\left(-\frac{\pi}{2} - \frac{a_2 L}{2\pi}\right). \tag{68}$$

One can verify that $\sigma_2 \in [\pi, 2\pi]$. If $\sigma_2 = 3\pi/2$, the point of arc-length $s = (L/2\pi)(\alpha + \sigma_2)$ is an inflection point of the AFM. If $\sigma_2 \neq 3\pi/2$, Equ. (68) admits two distinct solutions. The solution with $\sigma_2 \in [\pi, 3\pi/2)$ corresponds to a local maximum $s^{(2)}_{max}$, while the solution with $\sigma_2 \in (3\pi/2, 2\pi]$ corresponds to a local minimum $s^{(2)}_{min}$.

The relative location of the local minima, maxima, and inflection points, when they exist, is given by: $0 < s^{(1)}_{max} \le s_1 \le s^{(1)}_{min} \le s^{(2)}_{max} \le s_2 \le s^{(2)}_{min} < L$.

F. Proof of Property 2

The proof of Property 2 consists of bounding the local maxima of the abscissa $x(s)$ of $\mathbf{r}(s)$ in the second half portion of the AFM's spine. It makes use of the results established in Appendices C and E.

Property 2: *Let $\theta_0 = 0$ and $\varphi = 0$. Let $x(s)$ denote the x coordinate of $\mathbf{r}(s)$. If $x(L) \le L/2$, then $x(s) \le L/2$ for all $s \in [0, L]$.*

Proof: (We recall that the plane $\mathcal{P}$ is perpendicular to the x-axis.) Let $x(s)$ denote the abscissa of $\mathbf{r}(s)$. From Equ. (9) we have that $x(s) = a\int_0^s \cos\theta(u)du$. Proving Property 2 is equivalent to showing that, if $x(L) \le L/2$, then $x(s) \le L/2$ for all $s \in [0, L]$.

We first consider the case where $a = 1$ (*i.e.*, $b = 0$). Then the AFM lies in the plane $z = 0$. Intuitively, this corresponds to the worst case regarding the above property since none of the AFM length is "consumed" along the z-axis.

By hypothesis, both $x(0)$ and $x(L)$ are bounded by $L/2$. In Appendix D we established that $x(s)$ has at most two local maxima, at $s = s^{(1)}_{max}$ and $s = s^{(2)}_{max}$. Moreover we also showed that $x(s^{(1)}_{max}) \le L/2$. So, all it remains to do is to show that $x(s^{(2)}_{max}) \le L/2$ when $x(L) \le L/2$.

In the following we consider two state vectors $(a_1, a_2, 0, 0, 0)$ and $(a_1, 0, 0, 0, 0)$, both with the same values of a_1. We let $x(s)$ and $\theta(s)$ denote the abscissa of $\mathbf{r}(s)$ and the orientation of the tangent at this point for the first state vector. We let $x_{a_2=0}(s)$ and $\theta_{a_1=0}(s)$ denote the same parameters for the second state vector.

¿From the direct kinematic equation (18) and the fact that the Bessel function J_0 is strictly decreasing in $[0, \mu_0]$, we derive $x_{a_2=0}(L) \ge x(L)$, *i.e.*:

$$\int_0^L \cos\theta_{a_2=0}(s)\ ds \quad \ge \quad \int_0^L \cos\theta(s)\ ds. \tag{69}$$

For $s \in [s^{(2)}_{max}, L]$, both $\theta(s)$ and $\theta_{a_2=0}(s)$ belong to the interval $[-\pi, 0]$. Equ. (13) entails that $\theta(s) \ge \theta_{a_2=0}(s)$. Thus, we have $\cos\theta(s) \ge \cos\theta_{a_2=0}(s)$ for all $s \in [s^{(2)}_{max}, L]$, and:

$$\int_{s^{(2)}_{max}}^L \cos\theta(s)\ ds \quad \ge \quad \int_{s^{(2)}_{max}}^L \cos\theta_{a_2=0}(s)\ ds. \tag{70}$$

Combining Equ. (69) and (70), we get:

$$x(s^{(2)}_{max}) = \int_0^{s^{(2)}_{max}} \cos\theta(s)\ ds \le \int_0^{s^{(2)}_{max}} \cos\theta_{a_2=0}(s)\ ds = x_{a_2=0}(s^{(2)}_{max}). \tag{71}$$

This inequality gives an upper-bound of the abscissa of the second local maximum when $a_2 \ne 0$ in terms of the abscissa of the point with the same arc-length along the AFM when $a_2 = 0$.

We now show that $x_{a_2=0}(s^{(2)}_{max}) < L/2$. Since $s^{(2)}_{max}$ is the arc-length of the second local maximum of $x(s)$, we must have $\sqrt{a_1^2+a_2^2} \geq \pi^2/L + a_2$ (see Appendix E), which implies that $a_1 \geq \pi^2/L$. The condition $a_1 \geq \pi^2/L$ implies in turn that $x_{a_2=0}(s)$ has two local maxima, which we denote by $\tilde{s}^{(1)}_{max}$ and $\tilde{s}^{(2)}_{max}$. Then, obviously, we have that $x_{a_2=0}(s^{(2)}_{max}) \leq \max\{x_{a_2=0}(\tilde{s}^{(1)}_{max}), x_{a_2=0}(\tilde{s}^{(2)}_{max}), x(L)\}$. We now show that each of the terms $x_{a_2=0}(\tilde{s}^{(1)}_{max})$, $x_{a_2=0}(\tilde{s}^{(2)}_{max})$, and $x(L)$ is upper-bounded by $L/2$:

a. Since $a_1 > \pi^2/L$ and J_0 is strictly decreasing over $[0, 1]$, we have that $J_0(a_1L/2\pi) < J_0(\pi/2) < 1/2$, which yields $x_{a_2=0}(L) = LJ_0(a_1L/2\pi) < L/2$.

b. Since $\tilde{s}^{(1)}_{max} \in [0, L/2]$, we have: $x_{a_2=0}(\tilde{s}^{(1)}_{max}) < L/2$.

c. In Appendix E we established that $L/2 < \tilde{s}^{(2)}_{max} < s_2$, where s_2 is the arc-length of the second inflection point of $x_{a_2=0}(s)$. In Appendix C we showed that $s_2 = 3L/4$. Therefore:

$$\Big(x_{a_2=0}(\tilde{s}^{(2)}_{max}) - x_{a_2=0}(L/2)\Big) + \Big(x_{a_2=0}(\tilde{s}^{(2)}_{max}) - x_{a_2=0}(3L/4)\Big) \quad < \quad L/4. \tag{72}$$

Combined with $x_{a_2=0}(L/2) = x_{a_2=0}(L)/2$ and $x_{a_2=0}(3L/4) = 3x_{a_2=0}(L)/4$ (see Appendix C), we get:

$$\begin{aligned} x_{a_2=0}(\tilde{s}^{(2)}_{max}) &< \frac{L}{8} + \frac{5}{8}x_{a_2=0}(L) = \frac{L}{8} + \frac{5}{8}LJ_0(\frac{a_1L}{2\pi}) \\ &< \frac{L}{8} + \frac{5}{16}L = \frac{7}{16}L \\ &< \frac{L}{2}. \end{aligned} \tag{73}$$

Hence, $x(s^{(2)}_{max}) < L/2$. The two local maxima of $x(s)$, when they exist, are upper-bounded by $L/2$.

We have assumed that $a = 1$. If $a < 1$ the property still holds. To see that, consider the influence of the parametrer a on the geometry of the AFM's spine. The x coordinate of any point of the AFM's spine is proportional to a. Since the equations $x'(s) = 0$ and $\kappa(s) = 0$ do not depend on the value of a, the arc-length values of the extrema of $x(s)$ are the same for all values of a, at fixed a_1 and a_2. We obtain that if the end-effector is in the maneuvering region then the extrema of $x(s)$ are bounded by the quantity $aL/2$. □

G. Proof of Property 3

Property 3: *Let $b = 0$. Let $a_2 = 0$, $\theta_0 = 0$, and $\varphi = 0$. Let $x(s)$ denote the x-coordinate of $\mathbf{r}(s)$. If $x(L) > L/3$, then autocollision cannot occur.*

In Appendix C we saw that, when $a_2 = 0$, the inflection points of the AFM occur at $s_1 = L/4$ and $s_2 = 3L/4$.

When $a_2 = 0$, Equ. (41) and (42) yield:

$$x(L/2 + s) \quad = \quad x(L/2) + x(s), \tag{74}$$

$$y(L/2 + s) \quad = \quad y(L/2) - y(s). \tag{75}$$

Also, when $a_2 = 0$, Equ. (13) implies that $\theta(s) = \theta(L/2 - s)$, for all $s \in [0, L/2]$. Using $\theta(s) = \theta(L/2 - s)$ in Equ. (9) and integrating we get:

$$x(s) + x(L/2 - s) = x(L/2), \tag{76}$$
$$y(s) + y(L/2 - s) = y(L/2). \tag{77}$$

Using Equ. (74), (75), (76) and (77), we finally get:

$$x(L/2) - x(L/2 - s) = x(L/2 + s) - x(L/2), \tag{78}$$
$$y(L/2 + s) = y(L/2 - s). \tag{79}$$

showing that the AFM is symmetric relative to the plane $x(L/2)$.

When $a_2 = 0$, $\theta(s) \in [0, \pi]$ for all $s \in [0, L/2]$. Hence, $y(s)$ increases monotonically in the first half portion of the curve. By symmetry $y(s)$ decreases monotonically in the second half portion of the curve. Then, it is clear that autocollision can not occur between two points of the same half portion of the curve. Autocollision will occur when $x(s^{(1)}_{max}) \geq x(s^{(2)}_{min})$ (the second half portion of the curve penetrates the first half portion), and only in that case. Let x_a the x coordinate of the end-effector when $x(s^{(1)}_{max}) = x(s^{(2)}_{min})$. When $x = x_a$ we have $x(s^{(1)}_{max}) = x(L/2)$. Using Equ. (62), (63), and (64), we have: $x(s_1) = x_a/4$, $x(s^{(1)}_{max}) = x_a/2$. Combined with $s^{(1)}_{max} < s_1$ and $s_1 = L/4$, we get: $x_a/2 = x(s^{(1)}_{max}) < s^{(1)}_{max} < s_1 - x_a/4 = L/4 - x_a/4$, and finally we obtain the bound $x_a < L/3$. □